

A comparison of numerical surface topography calculations in geodynamic modelling: an evaluation of the ‘sticky air’ method

F. Crameri,¹ H. Schmeling,² G. J. Golabek,^{1,3} T. Duretz,¹ R. Orendt,² S. J. H. Buiter,^{4,5}
D. A. May,¹ B. J. P. Kaus,^{1,6} T. V. Gerya¹ and P. J. Tackley¹

¹ETH Zurich, Institute of Geophysics, Geophysical Fluid Dynamics, Sonneggstrasse 5, 8092 Zurich, Switzerland. E-mail: fabio.crameri@erdw.ethz.ch

²Goethe University, Institute of Earth Sciences, Altenhöferallee 1, 60438 Frankfurt am Main, Germany

³ENS Lyon, Laboratoire des Sciences de la Terre, 46 Allée d’Italie, 69364 Lyon Cedex 07, France

⁴Geological Survey of Norway, Leiv Eirikssons vei 39, 7491 Trondheim, Norway

⁵University of Oslo, Physics of Geological Processes, Sem Selands vei 24, 0316 Oslo, Norway

⁶Johannes Gutenberg University Mainz, Institute of Geosciences, J.-J.-Becher-Weg 21, 55099 Mainz, Germany

Accepted 2012 January 16. Received 2011 November 11; in original form 2011 June 17

SUMMARY

Calculating surface topography in geodynamic models is a common numerical problem. Besides other approaches, the so-called ‘sticky air’ approach has gained interest as a free-surface proxy at the top boundary. The often used free slip condition is thereby vertically extended by introducing a low density, low viscosity fluid layer. This allows the air/crust interface to behave in a similar manner to a true free surface. We present here a theoretical analysis that provides the physical conditions under which the sticky air approach is a valid approximation of a true free surface. Two cases are evaluated that characterize the evolution of topography on different timescales: (1) isostatic relaxation of a cosine perturbation and (2) topography changes above a rising plume. We quantitatively compare topographies calculated by six different numerical codes (using finite difference and finite element techniques) using three different topography calculation methods: (i) direct calculation of topography from normal stress, (ii) body-fitting methods allowing for meshing the topography and (iii) Lagrangian tracking of the topography on an Eulerian grid. It is found that the sticky air approach works well as long as the term $(\eta_{st}/\eta_{ch})(h_{st}/L)^3$ is sufficiently small, where η_{st} and h_{st} are the viscosity and thickness of the sticky air layer, and η_{ch} and L are the characteristic viscosity and length scale of the model, respectively. Spurious lateral fluctuations of topography, as observed in some marker-based sticky air approaches, may effectively be damped by an anisotropic distribution of markers with a higher number of markers per element in the vertical than in the horizontal direction.

Key words: Numerical solutions; Numerical approximations and analysis; Geomechanics; Tectonics and landscape evolution; Dynamics of lithosphere and mantle.

1 INTRODUCTION

Topography is a direct observable of the interaction between the Earth’s internal and external dynamics. The study of the processes affecting topography is, therefore, a very active research field and many studies have highlighted the importance of the feedback between surface processes and lithosphere dynamics (Koons 1989; Willett 1999; Schmeling *et al.* 2008; Braun & Yamato 2010). Coupling of regional geodynamic models with landscape evolution models is often used to study the behaviour of such a complex system (Braun 2006). Therefore, it is important for numerical models of Earth deformation to produce realistic topography.

Most mantle convection simulations until now treat the surface as a free-slip boundary. The Earth’s surface, however, is a free surface, which implies that both normal and shear stress should vanish at

this interface. Moreover, it has been shown that treating the Earth’s surface as a free surface can have a significant effect on lithospheric and mantle dynamics (Zhong *et al.* 1996; Kaus *et al.* 2008, 2010).

In the following paragraphs, we will give a short overview of the methods used to describe the surface evolution in geodynamic models. Topographic calculations in geodynamic modelling involve either direct calculation of topography from (1) normal stress, (2) body-fitting methods allowing for meshing the topography or (3) Lagrangian tracking of the topography on an Eulerian grid. In the mantle convection community, the deformation of the Earth’s surface has traditionally been studied using the normal stress method: Model setups usually involve a free-slip upper boundary condition and the topography is calculated as the compensation altitude that balances the normal stress acting at the top of the domain (McKenzie 1977; Blankenbach *et al.* 1989; Zhong & Gurnis

1992; Zhong *et al.* 1993). Topography behaves dynamically and evolves proportionally with stresses resulting from mantle dynamics (Hager *et al.* 1985). Further improvements were made to take the history-dependent feedback of topography on the interior dynamics into account (Gurnis *et al.* 1996; Zhong *et al.* 1996). This methodology involves the contribution of the normal topographic stresses on the upper Eulerian nodes into the next velocity field evaluation.

The second approach known as body-fitting methods provides a direct treatment of a free surface. This method enables the numerical grid to follow the topography; a zero normal stress condition can then naturally be applied on this surface. Such configuration can be achieved by either using a deforming Lagrangian grid (Melosh & Raefsky 1980; Poliakov & Podladchikov 1992; Hassani & Chéry 1996; Lavier *et al.* 2000; Crook *et al.* 2006, and references therein) or by using an Arbitrary Lagrangian-Eulerian (ALE) formulation that allows the Eulerian computation grid to adjust to the surface throughout deformation (Fullsack 1995). The main inconvenience of the Lagrangian approach remains the necessity of remeshing (regridding) in large deformation experiments (Poliakov & Podladchikov 1992; Fullsack 1995; Kaus *et al.* 2008; Quinteros *et al.* 2009). ALE methods can achieve large deformations without grid distortion and do not need regridding (e.g. Beaumont *et al.* 1994; Pysklywec *et al.* 2000; Quinquis *et al.* 2011).

Other kind of methods employ an Eulerian grid for the flow problem discretization and an independent discretization for representing the free surface. For this purpose, the Marker-and-Cell method (Harlow & Welsh 1965), level-set functions (Mühlhaus *et al.* 2007; Braun *et al.* 2008) or hybrid methods (Samuel & Evonuk 2010) are commonly used in geodynamics. Free-surface tracking techniques allow for the identification of the cells in the flow grid that contain the interface. This allows a free-surface boundary condition to be applied to the interface cells within the Eulerian grid (Harlow & Welsh 1965; Braun *et al.* 2008).

Another free-surface approximation, the so-called ‘sticky air’ approach, has recently gained interest in the geodynamics community. This method requires the addition of a fluid layer in the model domain. The latter is used as a proxy for air (or water) and, thereby, requires a low density and a sufficiently small viscosity. Subsequently, the interface between the markers defining the crust and the air behaves similarly to a free surface (Zaleski & Julien 1992; Gerya & Yuen 2003a; Schmeling *et al.* 2008; Quinquis *et al.* 2011). Since the model domain contains the surface of interest, this approach does not necessitate the application of a zero normal stress boundary condition. Sufficiently small normal stress at the surface is ensured by the physical properties of the air layer (density, viscosity), which, therefore, allows for the development of a realistic topography. In such methods, the location of the free surface on the flow grid is approximated proportionally with the spatial resolution of the markers. This is in contrast to body-fitting finite elements in which the boundary conditions can be exactly applied to the interface.

The sticky air method enables an easy implementation of a free surface in finite-difference (FD) or Eulerian finite-element (FE) codes. In this paper, we will focus on the practical use of the sticky air approach: A theoretical analysis will be presented that provides the physical conditions under which the sticky air approach is a valid approximation of a free surface. We will discuss two cases that characterize the evolution of topography on different timescales and will compare the topography obtained with six different numerical codes using all three described topography calculation methods among each other and against the theoretical prediction.

The further structure of the paper is the following. In Section 2, we describe the theoretical considerations on the validity of the sticky air approach, the governing equations and the model setups. Section 3 gives an overview of the numerical codes employed in this study, whereas Section 4 describes the results obtained. Finally, Section 5 features a discussion of the results and provides guidelines on how to use the sticky air approach properly.

2 THEORETICAL BACKGROUND

2.1 Analytical considerations

To simulate a free surface with a sticky air approach, the layer has to fulfil certain conditions, because any flow within it is associated with flow stresses. The free-surface conditions can be derived subject to the requirement that the sticky air layer allows vertical movements of the physical surface without exerting stresses on it. Any vertical deflection of the surface has to be able to relax isostatically without ‘feeling’ the presence of the sticky air layer.

A narrow deflection with amplitude $h_{\text{top},0}$ of wavelength λ at the top border of a box of width L causes a characteristic stress

$$\sigma_{\text{ch}} = \rho g h_{\text{top},0}, \quad (1)$$

where ρ is the density of the layer beneath the surface and g is the gravitational acceleration. Assuming a thin sticky air layer ($h_{\text{st}} \ll L$) mass conservation of sticky air may be written in terms of a vertically averaged horizontal velocity \bar{v}_x within the sticky air layer,

$$\frac{\partial \bar{v}_x}{\partial x} = -\frac{v_{\text{top}}}{h_{\text{st}}}, \quad (2)$$

where x is the horizontal coordinate and v_{top} is the vertical characteristic velocity of the crustal layer-sticky air boundary resulting from the geodynamic process under consideration. Identifying \bar{v}_x with the sticky air velocity v_{st} and integration gives,

$$v_{\text{st}} = -\int_x v_{\text{top}} \frac{dx}{h_{\text{st}}}. \quad (3)$$

As the sticky air layer is thin (having a free slip top), flow within it can be approximated with a channel flow of thickness $2h_{\text{st}}$ (having zero shear stress at the centre) resulting in,

$$v_{\text{st}} = -\frac{h_{\text{st}}^2}{3\eta_{\text{st}}} \frac{dP}{dx}, \quad (4)$$

where η_{st} is the sticky air viscosity and P is the pressure within the sticky air layer (Turcotte & Schubert 2002). Integration of eq. (4) using eq. (3) gives a characteristic pressure difference between $x = 0$ and $x = \lambda/4$;

$$\Delta P_{\text{ch}} = \frac{3\eta_{\text{st}}}{h_{\text{st}}^3} \int_{x=0}^{x=\lambda/4} \int_x v_{\text{top}} dx' dx. \quad (5)$$

As the normal deviatoric stress inside the sticky air layer is zero at the no-slip boundary, ΔP_{ch} is the only normal stress component acting on the surface of the medium. Defining the parameter C_{max} by

$$\Delta P_{\text{ch}} = C_{\text{max}} \sigma_{\text{ch}}, \quad (6)$$

we arrive at

$$C_{\text{max}} = \frac{3\eta_{\text{st}}}{h_{\text{st}}^3 \rho g h_{\text{top},0}} \int_{x=0}^{x=\lambda/4} \int_x v_{\text{top}} dx' dx. \quad (7)$$

The general condition for a traction free surface can thus be defined by

$$C_{\text{max}} \ll 1. \quad (8)$$

This condition can easily be applied to a specific model with regards to the timescale of its characteristic geological processes (see Section 5.6). Here, we discuss two cases considering short timescale (isostatic relaxation) and long timescale (rise of a plume) processes.

2.1.1 Isostatic timescale

A deflection with amplitude $h_{\text{top},0}$ of wavelength λ described by,

$$h_{\text{top}} = h_{\text{top},0} \cos\left(\frac{2\pi x}{\lambda}\right), \quad (9)$$

causes a characteristic stress described in eq. (1). The isostatic relaxation time of an infinite half-space of such a deflection is given by

$$t_{\text{rlx}} = \frac{4\pi\eta_{\text{ch}}}{\rho g \lambda}, \quad (10)$$

where η_{ch} is the viscosity controlling the relaxation (Turcotte & Schubert 2002) and here given by the mantle viscosity η_M . Combining eqs (1), (9) and (10) and dividing distance by time we obtain the vertical relaxation velocity

$$v_{\text{top}} = \frac{-h_{\text{top}}}{t_{\text{rlx}}} = \frac{-\sigma_{\text{ch}}\lambda}{4\pi\eta_{\text{ch}}} \cos\left(\frac{2\pi x}{\lambda}\right). \quad (11)$$

Combining with eq. (7), using the characteristic pressure difference between $x = 0$ and $x = \lambda/4$ and accounting for the characteristic wavelength in the model, which is here given by $\lambda = L$, where L is the box width, we arrive at

$$C_{\text{isost}} = \frac{3}{16\pi^3} \left(\frac{L}{h_{\text{st}}}\right)^3 \frac{\eta_{\text{st}}}{\eta_{\text{ch}}}, \quad (12)$$

with the condition for a traction free surface on isostatic timescales defined by

$$C_{\text{isost}} \ll 1. \quad (13)$$

2.1.2 Stokes timescale

A less restrictive condition may be formulated based on negligible dynamic sticky air pressure associated with topography variation on geologic timescales characterized by gravity driven movements of geological units of length scale l and density contrast $\Delta\rho$ (e.g. diapirs, slabs). To derive this condition the isostatic relaxation time (eq. 10) is replaced by the Stokes timescale

$$t_{\text{Stokes}} = \frac{h_{\text{model}}}{v_{\text{Stokes}}} = \frac{h_{\text{model}}\eta_{\text{ch}}}{Al^2g\Delta\rho}, \quad (14)$$

where v_{Stokes} is the Stokes velocity of the active geodynamic body, h_{model} is the height of the model and A is a geometric constant (1/3 for a weak Stokes sphere; Turcotte & Schubert 2002). Replacing the length scale l by $c_l h_{\text{model}}$, choosing $c_l = 0.5$ as an upper bound and taking the characteristic stress associated with the actively moving body as $2l\Delta\rho g$ the vertical velocity of the topography is of the order

$$v_{\text{top}} = \frac{\sigma_{\text{ch}} A h_{\text{model}} \Delta\rho}{4\rho\eta_{\text{ch}}}. \quad (15)$$

Integrating eq. (2) and using eq. (4) gives

$$\frac{\lambda v_{\text{top}}}{4h_{\text{st}}} = \frac{h_{\text{st}}^2}{3\eta_{\text{st}}} \frac{dP}{dx} \approx \frac{h_{\text{st}}^2}{3\eta_{\text{st}}} \frac{\Delta P}{\lambda/4}. \quad (16)$$

Defining C_{Stokes} similarly as in eq. (6)

$$\Delta P_{\text{ch}} = C_{\text{Stokes}} \cdot \sigma_{\text{ch}} \quad (17)$$

and choosing for simplicity $\lambda = 2h_{\text{model}}$, we arrive at

$$C_{\text{Stokes}} = \frac{1}{16} \frac{\Delta\rho}{\rho} \left(\frac{h_{\text{model}}}{h_{\text{st}}}\right)^3 \frac{\eta_{\text{st}}}{\eta_{\text{ch}}}. \quad (18)$$

The condition for a traction free surface in the isostatic limit (on timescales larger than t_{rlx}) can thus be defined by

$$C_{\text{Stokes}} \ll 1. \quad (19)$$

2.2 Physical model

The case study is defined as a purely viscous fluid dynamic problem. Elastic effects, which might become important in the presence of a high viscosity lithosphere are not considered in this study for two reasons. (a) The stress relaxation time of the model described in the next paragraph is either on the order of, or smaller than the observation time ($De \leq 1$, where De is the Deborah number) and (b) only few participating codes have implemented elasticity. Nevertheless, elastic effects should be kept in mind for different geodynamical applications (Zhong 2002; Kaus & Becker 2007). We assume an incompressible fluid, in which the driving density fields are advected with the flow. The problem can, therefore, be described by the equations of conservation of mass

$$\frac{\partial v_i}{\partial x_i} = 0, \quad (20)$$

the equation of momentum

$$-\frac{\partial P}{\partial x_i} + \frac{\partial}{\partial x_j} \left[\eta_k \left(\frac{\partial v_i}{\partial x_j} + \frac{\partial v_j}{\partial x_i} \right) \right] - \rho_k g \hat{z}_i = 0 \quad (21)$$

and the advection equation

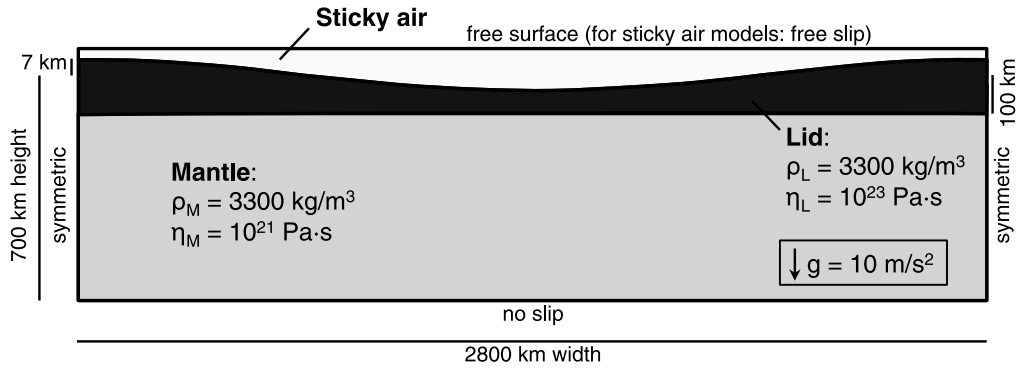
$$\frac{\partial c_k}{\partial t} + v_i \frac{\partial c_k}{\partial x_i} = 0, \quad (22)$$

where \vec{v} is the velocity, P the pressure, η_k the viscosity of composition k , \hat{z} the unit vector in vertical upward direction, ρ_k the density of composition k and c_k the concentration of composition k (either 0 or 1). The viscosity and the density depend on c_k and are, thus, also advected with the flow.

2.3 Model setups

The 2-D model setups for cases 1 and 2 are shown in Figs 1(a) and (b), respectively. In both cases, the model box spans 2800 km by 700–1100 km (greater model height is necessary in codes employing sticky air on top). For both cases, the initial condition is specified by a mantle of 600 km thickness, overlain by a cosine shaped, 93–107-km-thick lithosphere in Case 1, whereas it is 100-km-thick lithosphere in Case 2. The sticky air layer has a thickness varying between 10 and 400 km. The lithosphere is a highly viscous, dense medium ($\rho_L = 3300 \text{ kg m}^{-3}$, $\eta_L = 10^{23} \text{ Pa s}$). The underlying ambient mantle has a density of $\rho_M = 3300 \text{ kg m}^{-3}$ and a viscosity of $\eta_M = 10^{21} \text{ Pa s}$. For Case 2, we employ a plume with a radius of $r_P = 50 \text{ km}$, a density of $\rho_P = 3200 \text{ kg m}^{-3}$ and a viscosity of $\eta_P = 10^{20} \text{ Pa s}$. The plume centre is initially located 1400 km away from the side boundaries and 300 km above the bottom in the middle of the mantle layer. The sticky air layer on the top has a density of $\rho_{\text{st}} = 0 \text{ kg m}^{-3}$ and a viscosity of $\eta_{\text{st}} = 10^{18}–10^{20} \text{ Pa s}$ and is bordered by a

(a) 2-D cosine perturbation:



(b) 2-D Stokes cylinder:

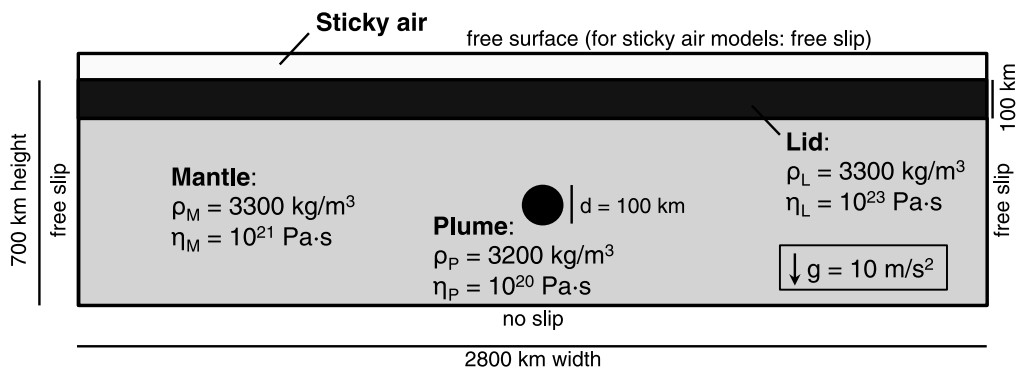


Figure 1. Model setup and initial condition for both 2-D cases employed in the study, where (a) Case 1 is featuring a cosine perturbation of the surface and (b) Case 2 includes a rising plume beneath the lithosphere.

free-slip top boundary condition. The mechanical boundary conditions at the sides are symmetric for Case 1. Periodic boundaries and a sinusoidal shaped topography could instead be used here for an equivalent result. Symmetric (reflective, free slip) side boundaries are used for Case 2. For both cases the bottom boundary is set to no slip condition. The setup for the real free-surface model is identical to the setup described earlier, except that the weak surface layer is removed, and the surface boundary condition used is zero normal stress.

2.4 Analytical solution for Case 1

The analytical solution for Case 1 assumes a three-layer model (Ramberg 1967). The upper layer has an infinite overburden and a no-slip bottom and is here associated with the sticky air layer of finite height. The middle layer is the lithosphere and a sublithospheric mantle gives the lower layer (see Fig. 1 for the dimensions, viscosities and boundary conditions). The maximum topography in Case 1 at time t can be derived analytically using the relaxation rate γ and from the initial maximum topography h_{init}

$$h_{\text{analytic}} = h_{\text{init}} \exp[\gamma t], \quad (23)$$

where $t = 14.825$ ka is the characteristic relaxation time and $\gamma = -0.2139 \times 10^{-11} \text{ s}^{-1}$ is the characteristic relaxation rate of the three-layer case at a given wavelength of 2800 km. It should be noted that these values are valid for infinitesimal amplitudes, whereas deviations are to be expected for small but finite amplitudes. In

particular, keeping the interface between the middle and lower layer flat and assuming a finite amplitude of the interface between the upper and middle layer implies that the thickness of the highly viscous middle layer varies laterally by ± 7 per cent (in the case of an initial maximum topography of 7 km). This variation increases the effective viscous flexural rigidity and leads to a slightly longer relaxation time.

2.5 Traction-derived topography at a free-slip surface

In this section, we briefly discuss the first method to calculate dynamic topography from normal stresses commonly used by the convection community (e.g. Burkett & Billen 2009). This method utilizes the vertical component of the stress vector (traction) at the vertically fixed, but horizontally free (free slip) surface. This approach is based on a Taylor series expansion of the vertical stress beneath a fully free surface. Let z_0 (positive upwards) be the fixed vertical position of the non-flexible surface of the convection model of vertical dimension L , and h be the real dynamic topography above z_0 of an equivalent model with a fully free surface. The xz - and zz -components of the stress tensor of the latter model at the position z_0 can be determined as a Taylor series about $z_0 + h$

$$\sigma_{xz}(z_0) = O\left(\frac{n_x}{n_z} \sigma_{\text{ch}}\right) + O\left(\frac{h}{L} \sigma_{\text{ch}}\right) + \text{HOT}, \quad (24)$$

$$\sigma_{zz}(z_0) = -\rho gh + O\left(\frac{n_x}{n_z}\sigma_{ch}\right) + O\left(\frac{h}{L}\sigma_{ch}\right) + \text{HOT}, \quad (25)$$

where ρ is the density near the surface, g is the gravitational acceleration, σ_{ch} is the characteristic stress associated with the flow, n_x and n_z are the horizontal and vertical components of the unit normal vector at the free surface and HOT are the higher order terms. Thus, n_x/n_z is the slope of the free surface. From eq. (24), we see that assuming a non-flexible free-slip surface is only justified if (a) the slope of the free surface is small ($\ll 1$) and (b) if the topography is sufficiently small ($h/L \ll 1$). Under these conditions, eq. (25) reduces to the usual traction derived dynamic topography to,

$$h = -\frac{\sigma_{zz}}{\rho g}. \quad (26)$$

It should be emphasized, that eq. (26) contains the full stress, including the dynamic pressure. Care has to be taken if lateral viscosity variations occur near the surface, which may deteriorate the pressure and thus topography (King 2009).

3 METHODS

3.1 Numerical details

The finite element codes MILAMIN_VEP, UNDERWORLD and SULEC provide calculations applying a true free surface, which are used as reference in the Case 2 setup. FDCON performs all the free slip cases. Sticky air results are provided by calculations of UNDERWORLD, SULEC, FDCON, I2VIS and STAGYY. All codes were extensively tested previously and provide runs at independent resolution. Resolution and further numerical details of each code are listed in Table 1.

Codes that use a sticky air layer and do not follow topography with a deforming Lagrangian grid, can either derive topography by

using a marker chain that follows the interface (SULEC, FDCON, I2VIS), by a set of passive markers that are initially defined on the interface and subsequently advected by the fluid flow (UNDERWORLD), or estimate topography from Eulerian nodes that read the compositional information (air or rock) from markers (STAGYY). Marker chains and passive markers are advected using the same techniques as compositional tracer advection and the precision depends, therefore, on the advection technique and the marker density along the chain. Similarly, the precision of the STAGYY approach depends on the marker density within the cells.

3.2 Participating codes

3.2.1 MILAMIN_VEP

MILAMIN_VEP (used by authors Golabek and Kaus) is a finite-element (FE) code (see Kaus *et al.* (2008)), which uses the efficient method to construct the stiffness matrix described by Dabrowski *et al.* (2008). The code employs a velocity–pressure formulation for the mechanical equations, with quadrilateral elements using either quadratic shape functions for velocity and discontinuous linear shape functions for pressure (Q_2P_{-1}), or linear shape functions for velocity and a discontinuous constant pressure shape function (Q_1P_0). This latter element is used for the results presented here. A free-surface stabilization algorithm (FSSA) is applied (Kaus *et al.* 2010). Calculations using both element types and the FSSA yield very similar results to models without FSSA, but with sufficiently small time steps. The code is employed in a Lagrangian manner, in which the elements are deformed at each time step. If the elements are too distorted, remeshing is applied. Tracers are employed to track material properties. Material properties are computed from tracers by computing the dominant phase at each integration point, after which the integration point values are averaged over the element.

Table 1. Numerical setups used in this work.

Detail	MILAMIN_VEP	SULEC	UNDERWORLD	FDCON	I2VIS	STAGYY
Numerical method	FE	ALE	FE	FD	FD	FD
Top boundary	f.surf	st.air/f.surf	st.air/f.surf	st.air/f.slip	st.air	st.air
Case 1						
Grid points	561 × 141	401 × 386 ^a 401 × 201	560 × 320 256 × 64	251 × 81 -	751 × 394 ^b	512 × 128
Tracers	10'570'002	9 part./elem. 9 part./elem.	36 part./elem. 36 part./elem.	260 part./cell -	49 part./cell	100 part./cell
Sticky air n_z	–	25 ^c	40 ^c	10 ^c	49	16 ^c
Case 2						
Grid points	841 × 211	401 × 376 ^a 401 × 251	560 × 340 140 × 140^d	401 × 123 401 × 101	750 × 304 ^b	1024 × 256
Tracers	10'570'002	9 part./elem. 9 part./elem.	36 part./elem. 36 part./elem.	250 part./cell 142 part./cell	49 part./cell	100 part./cell
Sticky air n_z	–	31 ^c	42 ^c	15 ^c	38	32 ^c
Tracer distribution	Denser at box centre	Evenly	Evenly	Vertically 4 × denser	Evenly	Evenly
Viscosity averaging	Harmonic	Harmonic	(see Section 3.2.3)	Arithmetic	Arithmetic	Geometric
Topography tracking	Distorted L. grid	Marker chain stretched E. grid	Passive markers distorted L. grid	Marker chain normal stress	Marker chain	Markers

Note: FE, finite element; FD, finite difference; ALE, arbitrary Lagrangian Eulerian; f.surf, true free surface; f.slip, free slip; st.air, sticky air; E., Eulerian; L., Lagrangian.

^aDenoted are numbers used for a sticky air thickness of $h_{st} = 100$ km. 20 nodes per 50 km of additional sticky air thickness are added in the vertical direction.

^bDenoted are numbers used for a sticky air thickness of $h_{st} = 100$ km. The number of vertical gridpoints is adjusted to keep the resolution constant at $\Delta z = 2$ km.

^cDenoted are numbers used for a sticky air thickness of $h_{st} = 100$ km, which are for any given thickness: $n_{z,st} = n_z \cdot h_{st} / h_{model}$.

^dCovers (due to symmetry) only half of the domain width and would correspond to a full model resolution of 280×140 gridpoints.

Using tracers in combination with a Lagrangian FEM framework has the advantage that only local tracer coordinates are required (inside an element), since global coordinates can be retrieved by multiplying with the element shape function. Calculations for Case 1 are performed with a resolution of 561×141 nodes and for Case 2 841×211 nodes are used. Over 10 million tracers are implemented for both cases.

3.2.2 SULEC

SULEC (used by author Buitert) is an Arbitrary Lagrangian Eulerian finite-element code developed by Buitert and S.M. Ellis. It solves the equation for conservation of momentum for slow creeping flows under the condition of incompressibility (eqs 20 and 21). The equations are discretized on a Eulerian mesh built of quadrilateral elements, which use linear shape functions for velocity and constant pressure (Q_1P_0). We use the direct solver Pardiso (Schenk & Gärtner 2004). Pressure is computed as mean stress in an iterative penalty formulation (Pelletier *et al.* 1989). We present SULEC results for both a true free surface and for an approximation to a free surface by a sticky air layer. A true free surface is obtained by a slight vertical stretch of the Eulerian mesh to accommodate surface displacements and the effects of surface processes (Fullsack 1995). SULEC includes stabilization of interfaces with a strong density contrast, such as Earth's surface (Kaus *et al.* 2010; Quinquis *et al.* 2011). For models with a sticky air layer, we track the crust–air interface with a connected string of points (a marker chain of 1603 points). This string follows the top surface of the lithosphere and is, therefore, not disturbed by the high deformation rates that can occur in the ‘sticky air’. Material properties, stresses and strains are advected with tracer particles. The models in this study use harmonic averaging of viscosity from tracers to elements and arithmetic averaging for density. The resolution for Case 1 is 401×201 nodes with 1203×603 tracers and 401×251 nodes with 1203×753 tracers distributed over the lithosphere and mantle domain are used for Case 2. For setups using a sticky air layer, more nodes and particles are added in the vertical direction.

3.2.3 UNDERWORLD

UNDERWORLD (used by author May) is an open-source (<http://www.underworldproject.org>), geodynamic modelling framework capable of deriving viscous/visco-plastic thermal, chemical and thermochemical models consistent with tectonic processes, such as mantle convection and lithospheric deformation over long timescales. UNDERWORLD utilizes a parallel 2-D/3-D finite element discretization to solve the incompressible Stokes flow problem. Constitutive behaviour, material properties (e.g. viscosity, density) and history variables (e.g. plastic strain, elastic stress) are discretized via a swarm of Lagrangian markers (Moresi *et al.* 2003, 2007). The novelty of the marker approach used here is that the material points are also used as the quadrature points used to evaluate the element stiffness matrices which are a function of the constitutive behaviour and or, the material properties. Consequently, no interpolation is directly required between the marker properties and the finite element mesh. The saddle point problem arising from the discretization of the incompressible Stokes flow problem is solved using the Schur complement reduction (SCR) method. UNDERWORLD utilizes the Portable, Extensible Toolkit for Scientific Computation (PETSc; Balay *et al.* 2008) to provide support for parallel linear algebra, a wide range of Krylov subspace methods and direct solvers as well as multilevel pre-conditioners. The results

in Case 1 are performed using 560×320 (sticky air model) and 256×64 (true free-surface model) Q_1P_0 elements. The resolution for Case 2 is set to 560×340 (sticky air model) and 140×140 (true free-surface model) elements, where the latter setups cover only half of the domain. All models are run with 36 particles per element. In Case 2, the topography profile was determined using a set of passive markers initially located on the interface between the air and the crust. In both, the sticky air and the free-surface models, 5000 evenly spaced markers were used to track the topography. A direct solver is used for the velocity sub-problem which is required to be solved by SCR. All calculations are performed using version 1.5.0 of UNDERWORLD.

3.2.4 FDCON

The code FDCON (used by authors Schmeling and Orendt) is a finite difference code. Eqs (20) and (21) are rewritten as the bi-harmonic equation in terms of the stream function and variable viscosity (e.g. Schmeling & Marquart 1991). The FD formulation of the biharmonic equation results in a symmetric system of linear equations, which is directly solved by Cholesky decomposition. The advection equation is solved by a marker approach (e.g. Weinberg & Schmeling 1992). The region is filled with markers, which carry the information of composition k . The concentration c_k of composition k at any FD gridpoint is determined by the number of markers of composition k found within a FD-cell sized area around the gridpoint divided by the total number of markers present in the same cell. The density and viscosity at any gridpoint are determined by c_k -weighted averaging using the arithmetic mean. The markers are advanced by a fourth-order Runge–Kutta scheme, combined with a predictor–corrector step. For this predictor–corrector step, markers are provisionally advanced by two first-order Eulerian steps. The momentum equation is solved for these preliminary steps to obtain the corresponding velocity fields. These velocity fields are then taken for the full fourth-order Runge–Kutta step to advance the markers. Case 1 is resolved using 251×81 gridpoints with 1280×4120 markers. For Case 2, 401×123 gridpoints with 3200×3840 markers (sticky air model) and 401×101 gridpoints with 4800×1200 markers (free-slip model) are used.

3.2.5 I2VIS

I2VIS (used by authors Duretz and Gerya) is a thermo-mechanical code developed by Gerya & Yuen (2003b). This numerical code is based on conservative finite differences. The momentum equations are discretized on a Eulerian staggered grid and the resulting system of linear equations is then solved using the direct solver Pardiso (Schenk & Gärtner 2004). The advection equation is treated using a Lagrangian marker-and-cell technique. Each time step, the markers are advected using a fourth-order in space Runge–Kutta scheme. Mapping between Lagrangian markers and Eulerian nodes is carried out by mean of linear distance-weighted interpolation. In this paper, the nodal viscosities are computed as the arithmetic mean of the viscosity of the surrounding markers. Calculations for Case 1 are performed with a resolution depending on the sticky air thickness that uses up to 751×394 gridpoints. 750×304 gridpoints are used for Case 2. 7×7 markers per cell are used for both cases.

3.2.6 STAGYY

STAGYY (used by authors Cramer and Tackley) is a finite difference/finite volume code developed by Tackley (1993, 2008). The code solves the equations of highly viscous flow on a staggered

grid. A multigrid iterative solver is used. Tracer particles are used to track the different compositions, which are in this case sticky air, lid, mantle and plume in Case 2. Tracer advection is done by a fourth-order in space Runge–Kutta technique integrating the velocity field. The fraction of each material type in each grid cell is determined using the same method as in FDCON except using a linear weighting function to integrate over nearby tracers (Tackley & King 2003). Material properties density and viscosity are then calculated for each cell from the material fractions. Numerical experiments using the initial setup of Case 1 are performed using 512×128 gridpoints with 6.5 million tracers, whereas the resolution for Case 2 is set to 1024×256 gridpoints with 26 million tracers.

4 RESULTS

The results for both model setups (Cases 1 and 2) from the different numerical codes using different upper boundary descriptions are described in the following sections. A quantitative overview on the results including the according sticky air parameter and model resolution is given in Table S1.

4.1 Case 1

The Case 1 initial topography relaxes to equilibrium over about 100 ka. Fig. 2 shows the comparison of this topographic decay between the different free-surface approaches and the analytical solution (eq. 23). The results of the sticky air approach are given for identical layer thickness of 100 km but with different viscosity thereof (Figs 2a and b) and for different layer thickness and identical viscosity (Figs 2c and d). The results differ significantly depending on the parameters defining the weak air layer. Lithospheric deformation becomes increasingly difficult when decreasing the thickness of the air layer or when increasing its viscosity. The resulting topography (measured at the maximum topography) thus diverges from the analytical solution that is given after one relaxation time of 14.825 ka. This inaccuracy in topography of lithospheric adjustment arising from different parameters of the sticky air layer (h_{st} , η_{st}) is presented spatially in Fig. 3(a) and temporally in Fig. 3(b), both related to the relaxation time t_{rx} . Fig. 3(b) shows the relative errors at one relaxation time using an initial maximum topography of 7 km (solid lines). To check the validity of these results with respect to the initial amplitude of topography, further experiments were carried out using an order of magnitude smaller initial maximum topography of 700 m (dashed lines). Both cases are computed with identical resolution (see Table 1) and show good agreement.

The prediction of the sticky air quality depending on thickness and viscosity is given by eq. (12) with the condition of $C_{isost} \ll 1$ for suitable sticky air parameters (Fig. 3c). The comparison to the results presented in Figs 3(a) and (b) shows good agreement. Favourable weak layer thicknesses are, therefore, $h_{st} > 50$ km for $\eta_{st} = 10^{18}$ Pa s, $h_{st} > 110$ km for $\eta_{st} = 10^{19}$ Pa s and $h_{st} > 240$ km for $\eta_{st} = 10^{20}$ Pa s as indicated by the grey shaded areas in Fig. 3.

A sticky air that yields a C -value of $C > 1$ can significantly influence correct topography evolution and results in large errors. The errors for different C_{isost} values are shown in Fig. 4. The influence of the sticky air layer is minimized towards low C_{isost} values and becomes acceptable for $C_{isost} \ll 1$. The topography error of 100 m for the best case shown in Fig. 2(b) achieved by a C_{isost} value of ~ 0.1 can further be reduced to for example, 40 m at $C_{isost} = 10^{-2}$. The relative temporal error is reduced down to less than 0.2 per cent

for $C_{isost} = 10^{-2}$. The slight increase at lowest C_{isost} values is due to resolution: all cases shown in Fig. 4 are calculated using constant number of gridpoints, but the thickness of the sticky air layer and thus also the thickness of the model increase towards lower C_{isost} values. This shows the trade-off between physical accuracy and numerical expense and is discussed in Section 5.2.

4.2 Case 2

In Case 2, a buoyant body rises and approaches the lithosphere. After about 8–10 Ma it begins to flatten and spreads near the base of the lithosphere (Fig. 5). Although in Case 1 traction-derived topography at a free-slip surface is not possible, Case 2 allows us to compare this method with the other free-surface calculation methods. An analytical solution, on the other hand, is not available for this model and the results are, therefore, compared to a high resolution, true free-surface result of MILAMIN_VEP.

4.2.1 Topography at a free surface

The analytical prediction of eqs (18) and (19) is applied to the model of Case 2. Figs 6(a) and (c) show the long-term evolution of the maximum topography for the different codes compared to the real free-surface approach given by MILAMIN_VEP and the according versions of SULEC ('SULEC free surface') and UNDERWORLD ('UNDERWORLD free surface'). Again, experiments using a low viscosity and/or a thicker weak-surface layer perform better in converging to the real free-surface results. In contrast to Case 1, the longer lasting topography evolution is less sensitive to the sticky air parameters, which is also accounted for in the Stokes condition given in eq. (18). Results start to diverge from the true free-surface topography only when using a thin sticky air layer combined with a high sticky air viscosity (Fig. 6c). Short-term dynamics (e.g. isostatic adjustment) might be unresolved in these models, although the long-term condition is satisfied by the sticky air parameters if C_{Stokes} is less than 1 (Fig. 6d). Adjusting the sticky air parameters to a more restrictive condition than the one discussed earlier provides the resolution not only for the long-term geodynamics but also for the isostatic adjustment occurring in the beginning of the simulation (Fig. 6b). Using here sticky air parameters of $h_{st} = 150$ km and $\eta_{st} = 10^{18}$ Pa s satisfies both conditions ($C_{isost} = 0.04$ and $C_{Stokes} = 1.9 \times 10^{-4}$), whereas a sticky air using $h_{st} = 10$ km and $\eta_{st} = 10^{18}$ Pa s satisfies only the long-term ($C_{Stokes} = 0.65$) but not the short-term condition ($C_{isost} = 133$).

Snapshots of the viscosity field and of the surface topography at different times are given in Figs 5 and 7, respectively. The lithosphere starts to deflect shortly after the beginning of the plume rise and the point of maximum topography continues to uplift until about 17 Ma. Thereafter, the laterally spread plume is not able to maintain the weight of the lithospheric bulge, which subsequently starts to relax.

4.2.2 Traction derived topography at a free-slip surface

The black solid line in Figs 6(a) and (b) shows the traction-derived topography using eq. (26) of a Case 2 run without sticky air, that is, with a non-flexible free slip surface (FDCON, $n_x = 401$, $n_z = 101$, 4800×1200 markers). In contrast to the fully free-surface cases or the cases with sticky air, immediately at time 0 the topography is fully developed, that is, this approach fully missed the isostatic adjustment stage. In other words, using eq. (26) gives the dynamic

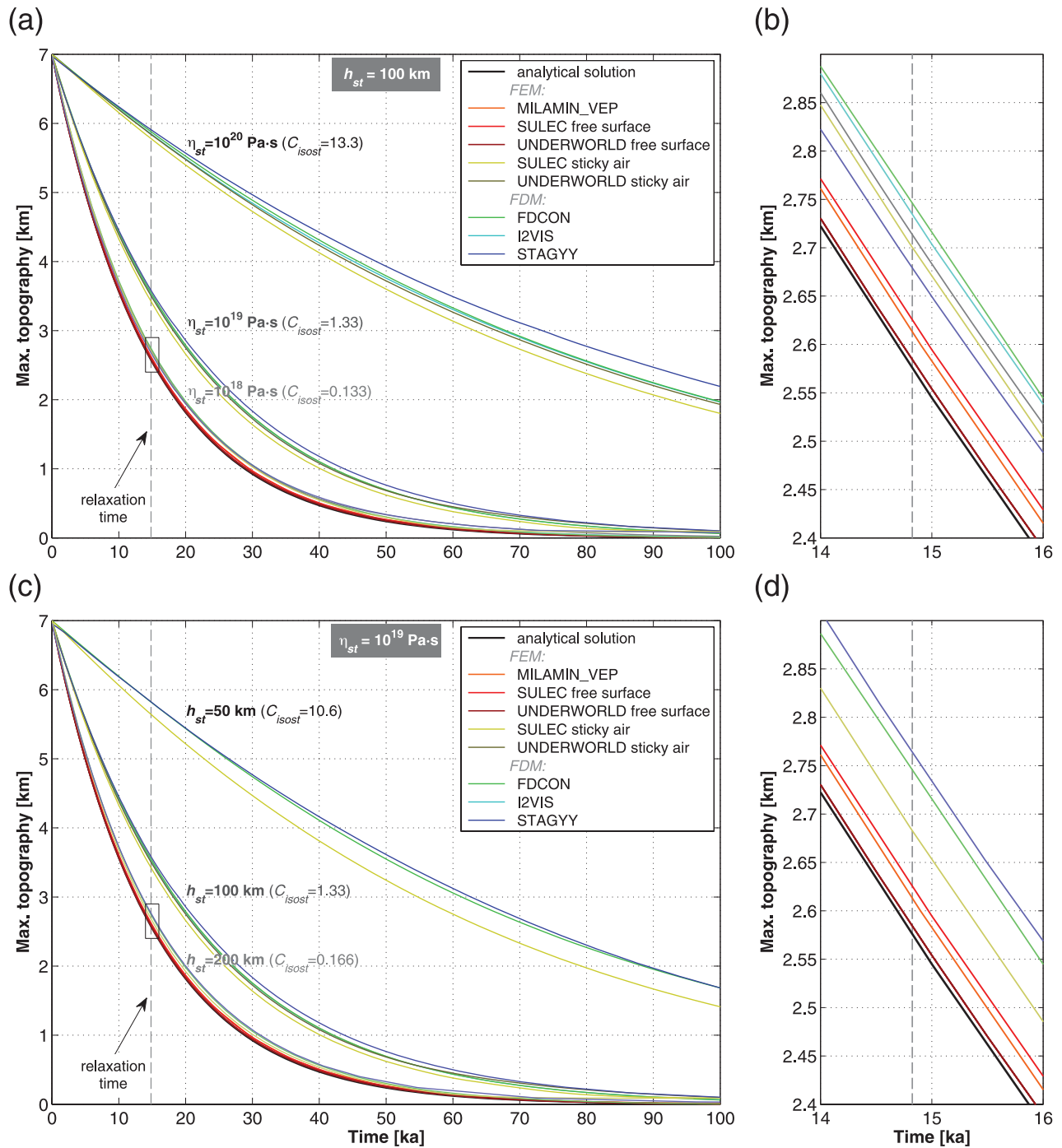


Figure 2. Maximum topography of Case 1 over time from the analytical solution (black), from three real free-surface simulations (reddish lines) and from the sticky air approach (coloured lines) shown for (a) a 100-km-thick layer and low, intermediate and high viscosities and for (c) a viscosity of $\eta_{st} = 10^{19}$ Pa·s and for thin, intermediate and thick sticky air layer thickness. (b, d) Close-up as marked by the square in (a, c). The relaxation time of 14.825 ka is indicated as dashed grey line and sticky air condition C_{isost} (eq. 12) is given for the different parameters.

topography always in the limit of instantaneous isostatic adjustment. The instantaneous reaction of tractions therefore causes the true topography to look temporarily delayed compared to the free slip result.

Secondly, the free-surface models show viscous bending during the early isostatic adjustment phase (not shown), that is, negative side lobes on both sides of the positive topography. Any topography associated with viscous plate bending cannot be captured with non-flexible traction derived topography models. At times longer than

the isostatic relaxation time there is good agreement with the sticky air and the fully free-surface models.

5 DISCUSSION

5.1 Time step requirements

A disadvantage of numerical calculation of viscous flow using either a free surface (Lagrangian FEM) or the sticky air approach is, that

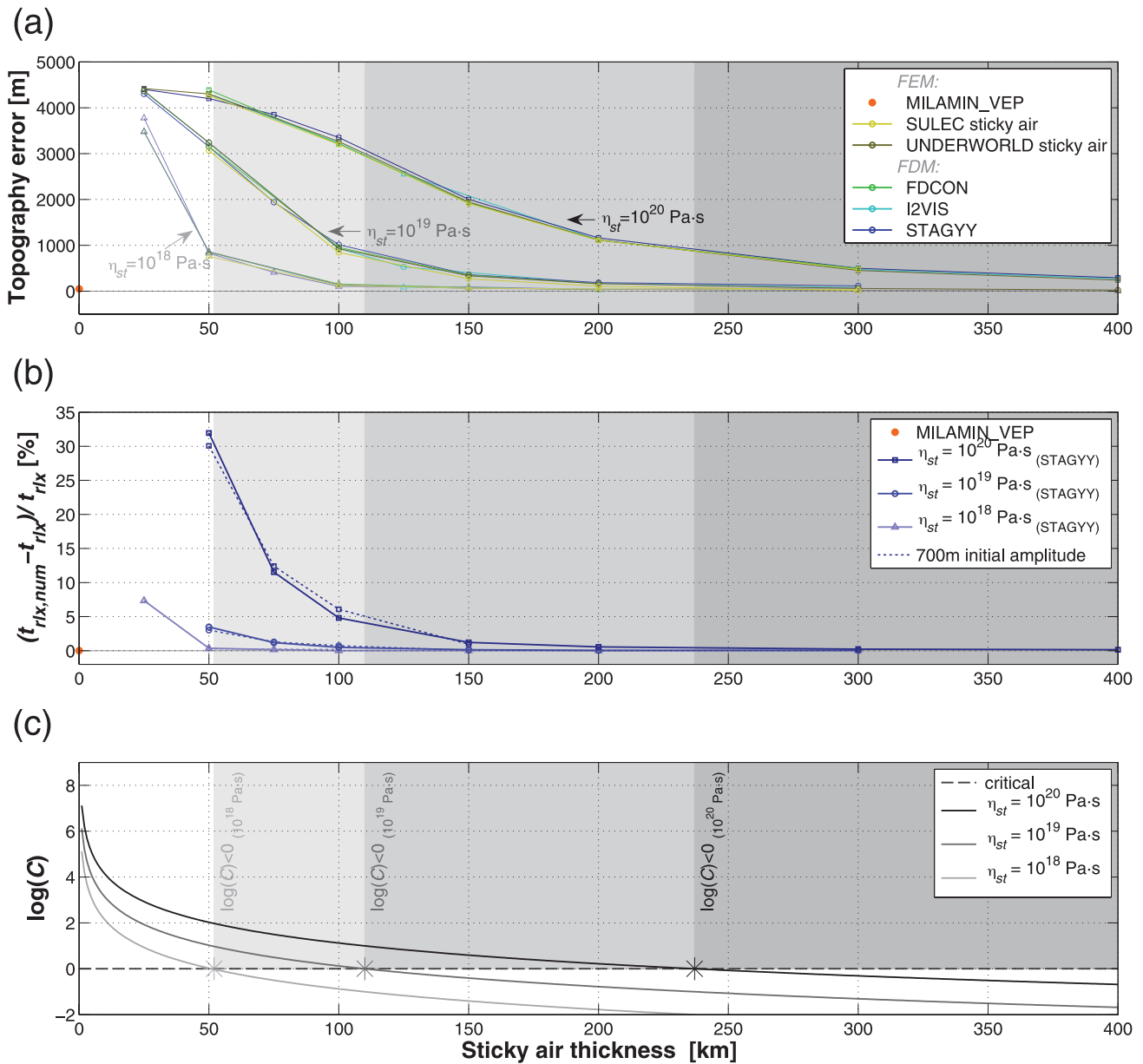


Figure 3. (a) Topography offset for different sticky air layer thickness at the characteristic time ($t_{rlx} = 14.825$ ka) for Case 1. (b) Relative temporal error between numerical ($t_{rlx,num}$) and analytical (t_{rlx}) relaxation time of reaching the analytically derived topography at t_{rlx} also shown for an initial topography of only 700 m height (dashed lines). (c) Analytical prediction of the quality of the free-surface approach given in eq. (12) (recommended if $C \ll 1$) and shown as according shaded areas. Curves show low (light colours) to high (dark colours) sticky air viscosity.

they may give rise to numerical oscillations related to time-step restrictions (Kaus *et al.* 2010; Quinquis *et al.* 2011). This effect may occur when advecting large density contrasts or a true free surface. To avoid such oscillations, usually the time step has to be chosen to be significantly smaller than the isostatic relaxation time (eq. 10). Kaus *et al.* (2010) derived a correction term to be added to the equation of momentum allowing for larger time steps (see also Duretz *et al.* 2011). This stabilization term is implemented in MILAMIN_VEP and SULEC.

Another approach to that problem is given by a more accurate, but more expensive calculation. It is done by the combination of a predictor-step with fourth-order Runge–Kutta advection as performed in FDCON (Schmeling *et al.* 2008, and see description in Section 3.2.4). With such a predictor step, the time step may exceed

the relaxation time by up to several times (e.g. Fuchs *et al.* 2011). In the present Case 2, the relaxation time is about 15 ka (*cf.* Case 1), and time steps up to 16–32 ka could be used to get non-oscillating stable results with FDCON.

5.2 Free-surface approach using sticky air

Apart from the points discussed in the previous section, a low sticky air viscosity reduces the advective time step due to higher velocities in the air layer and gives rise to numerical problems. On the other hand, as implied by our C -parameters, a high sticky air viscosity results in unphysical effects: the sticky air layer induces larger stresses on the surface that inhibit correct topography evolution.

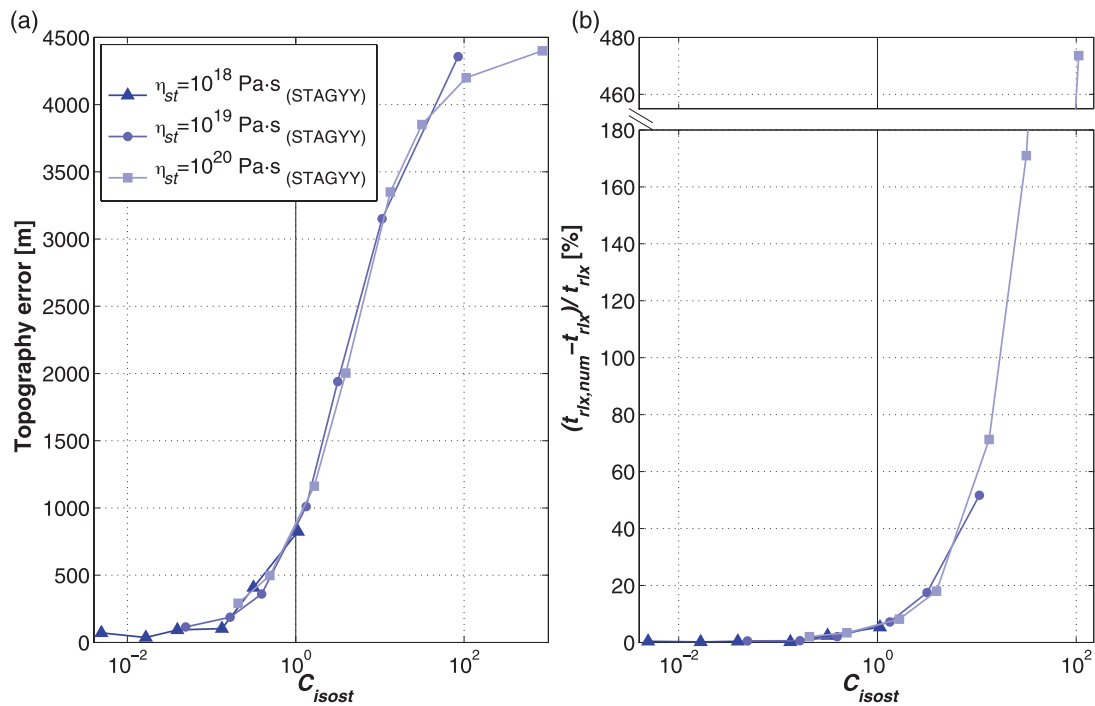


Figure 4. (a) Topography error and (b) relative temporal error $[(t_{rlx,num} - t_{rlx})/t_{rlx}]$ of Case 1 results (STAGYY) in dependence of C_{isost} (eq. 12). Errors are small for $C_{isost} \ll 1$.

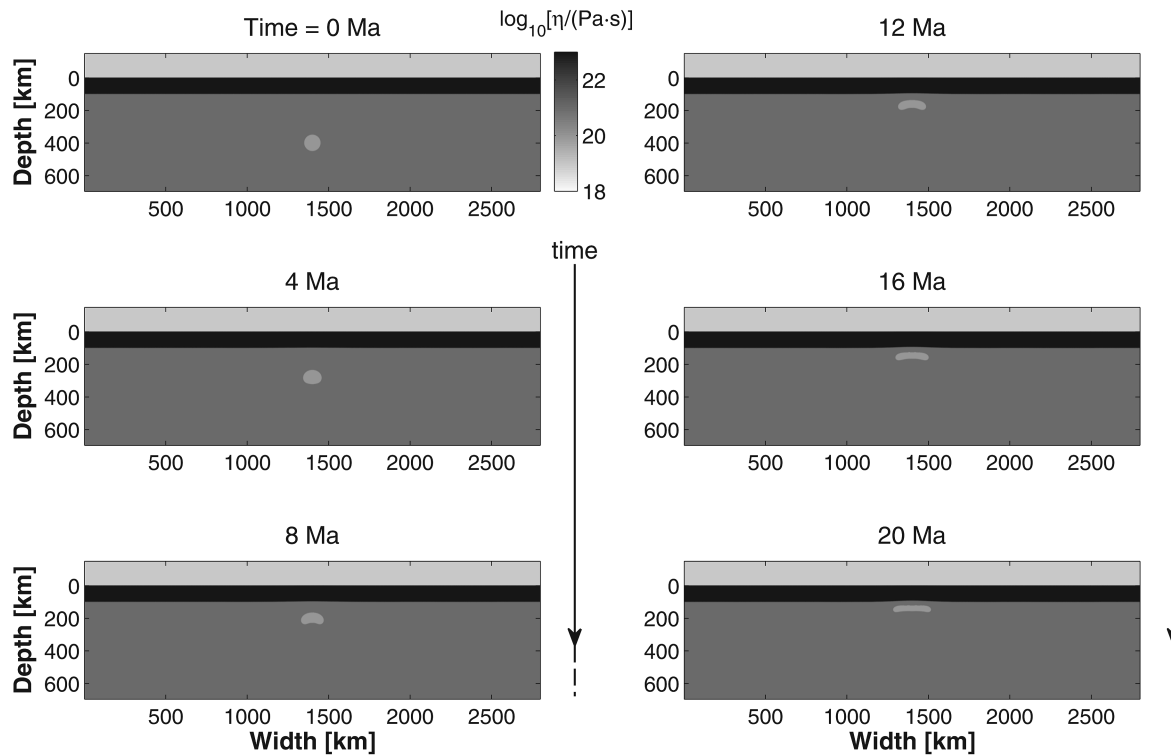


Figure 5. Temporal evolution of a Case 2 simulation calculated by STAGYY with $\eta_{st} = 10^{19}$ Pa s and $h_{st} = 150$ km shows the viscosity field at 0, 4, 8, 12, 16 and 20 Ma, indicated as dashed lines in Figs 6(a) and (c).

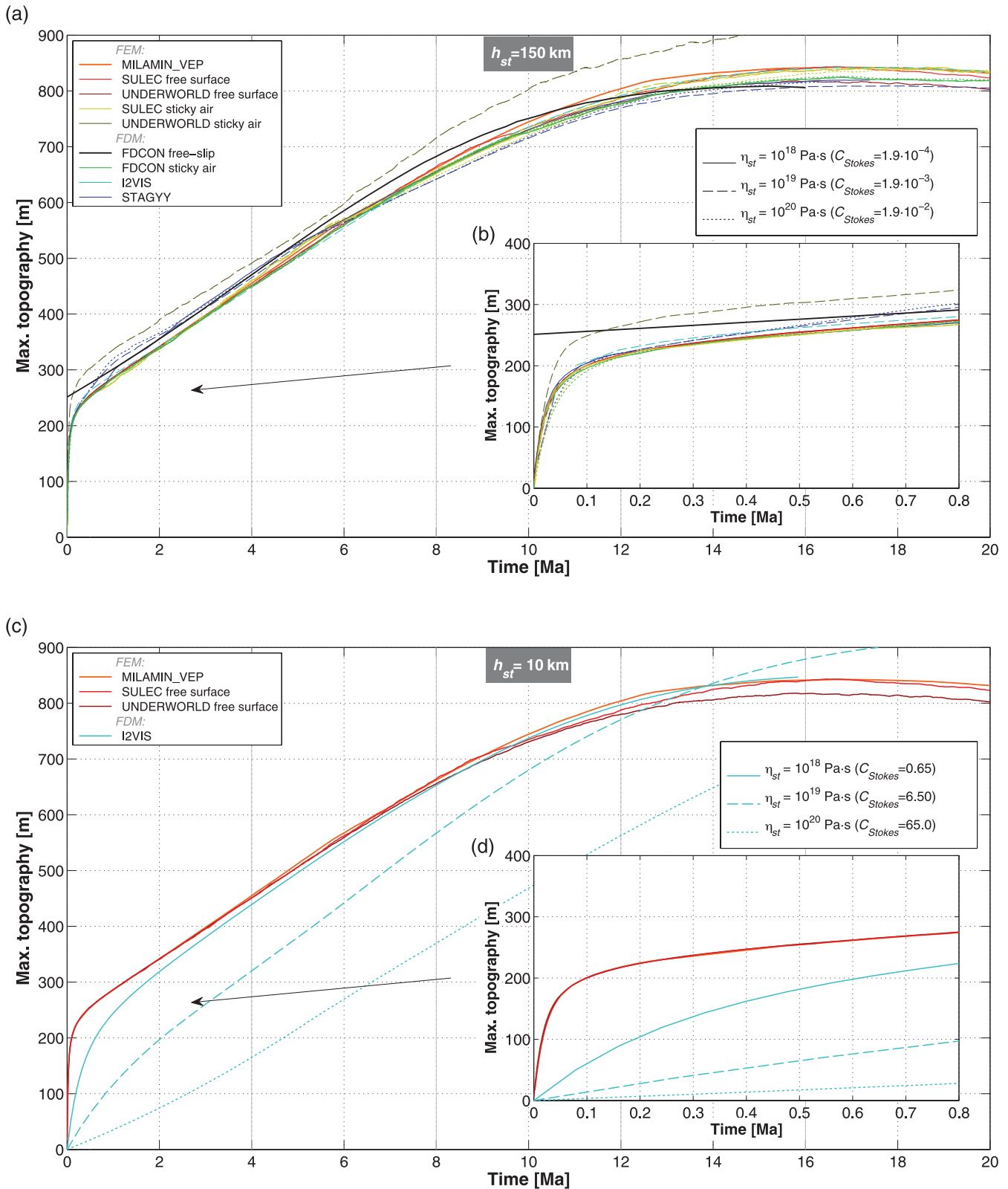


Figure 6. Maximum topography of Case 2 for three real free-surface simulations (reddish lines) and free-surface simulations using the sticky air (coloured lines) shown for (a,c) long-term evolution and (b,d) short term isostatic adjustment. (a,b) Comparison of a free-slip simulation (thick black line) and several sticky air results that use a 150 km thick weak surface layer and variable viscosity. (c,d) Sticky air results (I2VIS) using a 10 km thin weak surface layer and variable viscosity. The sticky air condition C_{Stokes} (eq. 18) is given for different parameter and is not satisfied for a sticky air viscosity of 10^{20} (dotted line) or 10^{19} Pa s (dashed line) but is satisfied for 10^{18} Pa s (solid line). The vertical grey lines indicate the time of the snapshots given in Figs 5 and 7.

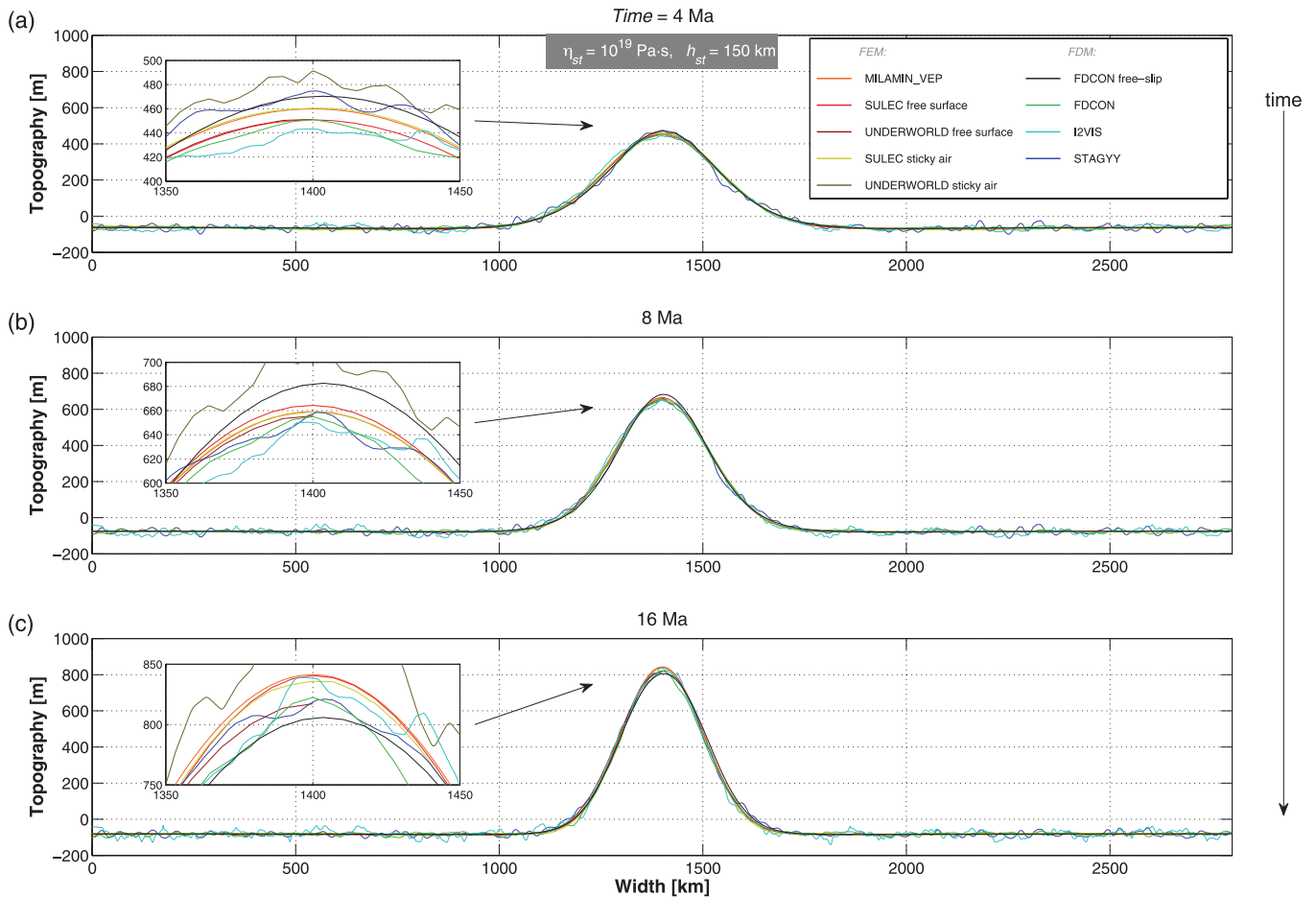


Figure 7. Surface topography comparison between three real free-surface simulations (reddish lines) and simulations using the sticky air approach (coloured lines) with $\eta_{st} = 10^{19}$ Pa s and $h_{st} = 150$ km at (a) 4 Ma, (b) 8 Ma and (c) 16 Ma. Small plots show zoom-in on the maximum topography.

If properly numerically resolved, a thicker sticky air layer can counteract these large stresses induced by its high viscosity to some degree. Deformation of the sticky air layer proceeds easier when its thickness is sufficiently large (see also Section 2.1 and Fig. 2c).

Topography evolving underneath a sticky air layer usually demands the resolution of different timescales. Short timescales (up to several kiloyears) comprising isostatic relaxation require a well-conditioned sticky air layer (see Figs 2 and 3). Long timescales (on the order of millions of years) given by the topographic signal of a rising plume are on the other hand less restrictive on the parameters defining a well suited sticky air layer (see Figs 6 and 8).

The close-ups in Fig. 2 show that the true free-surface models lie above the analytic solution by about 1–2 per cent whereas the sticky air models deviate by 4–6.7 per cent. We believe that the first deviation indicates that our highly viscous layer with ± 7 per cent thickness variations relaxes 1–2 per cent slower than a constant thickness layer as assumed in the analytic solution. The systematically higher values of the sticky air models indicates that the air still has a non-negligible influence at the parameter choices given in Fig. 2. Models having more suitable parameters are comparable to true free-surface models (e.g. $h_{st} = 200$ km, $\eta_{st} = 10^{18}$ Pa s with a deviation of 1.4 per cent).

5.3 Effect of numerical resolution

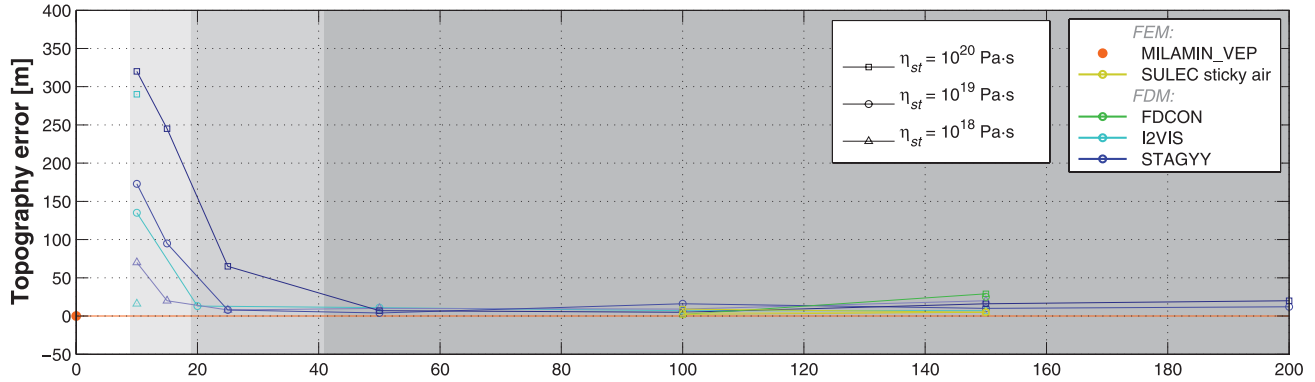
Additional experiments are performed using the Case 2 setup to test a possible influence of numerical setups on the accuracy of topog-

raphy. The results of I2VIS are presented for different resolution in space and time and are given in Tables 2 and 3, respectively. Spatial resolution is tested varying both, the number of gridpoints and the number of markers per cell. The resulting topography at 3 Ma is compared to the high resolution, true free-surface result of MILAMIN_VEP (Table 2). At low resolution, the topography at 3 Ma is overestimated by more than 100 m. An increase in either the number of markers per cell or the number of gridpoints can lead to better results that lie within a few metres range around the high-resolution true free-surface result. The variability in the metre-scale at high-resolution cases might be related to the fluctuation problem discussed in Section 5.4. A too-large time step can similarly influence the topographic evolution of the model. Constant time steps between 250 and 4000 yr are therefore tested for the Case 2 setup. In contrast to low spatial resolution, insufficient temporal resolution (i.e. using a large time step) does underestimate the true free-surface result at 3 Ma. The difference in topography is smaller and in the order of a few tens of metres.

5.4 The fluctuation problem

Using the marker approach and approximating the free surface by a sticky air layer, it is often observed that the surface becomes rough, exhibiting undesired spatial fluctuations. Fig. 7 shows that this effect also occurs in Case 2 with amplitudes of more than 100 m. Surprisingly, even in the absence of any driving force or buoyant bodies, fluctuations appear and increase asymptotically with time

(a)



(b)

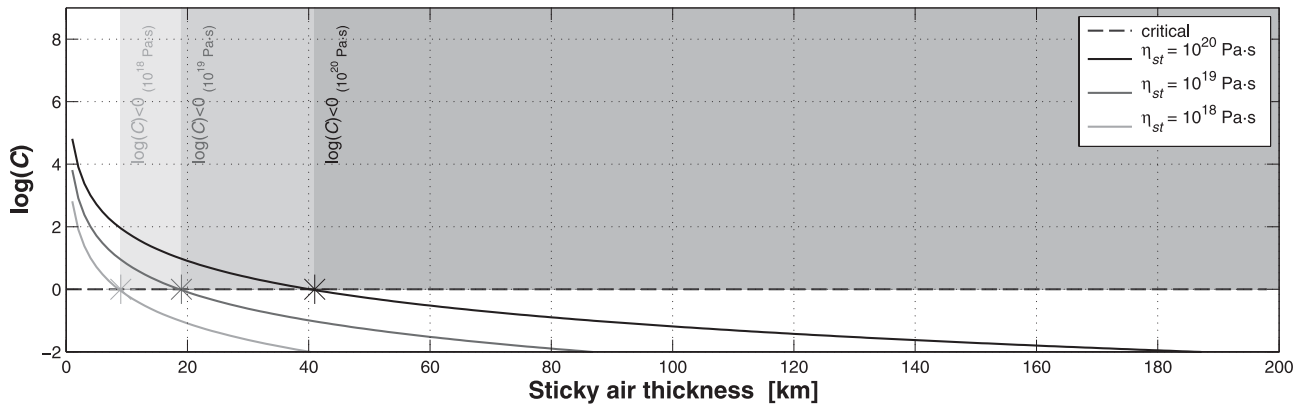


Figure 8. (a) Topography offset of sticky air approaches relative to highest resolution true free surface result (from MILAMIN_VEP) at 4 Ma for different sticky air layer thickness for Case 2. (b) Analytical prediction of the quality of the free-surface approach given in eq. (18) (recommended if $C \ll 1$) and shown as according shaded areas. Curves show low (light colours) to high (dark colours) sticky air viscosity.

Table 2. Spatial resolution test performed for different number of gridpoints and markers per cell. Shown are max. topography and the difference to the max. topography of the true free-surface result of MILAMIN_VEP.

		Max. topography (m) ^a /Topo. difference [m] ^b		
		Grid points		
		301 × 101	601 × 201	1201 × 401
Markers/cell	2 × 2	531/+133	425/+27	397/-1
	4 × 4	417/+19	381/-17	392/-6
	6 × 6	399/+1	394/-4	393/-5

Note: Time step: $\Delta t = 1000$ a.

Sticky air: $h_{st} = 100$ km; $\eta_{st} = 10^{18}$ Pa s ($C_{Stokes} = 6.5 \times 10^{-4}$).

^aFor Case 2 at $t = 3$ Ma using code I2VIS.

^bCompared to true free-surface result of MILAMIN_VEP (398 m).

into white noise fluctuations of the surface. Fig. 9 shows an example (FDCON, Case 2, no buoyant cylinder, $n_x = 421$, $n_z = 121$, 1280×2560 markers), in which this effect leads to topography fluctuations with amplitudes in the order of 50–80 m. Interestingly, the fluctuations start with a long wavelength, whereas shorter wavelengths form at later stages.

This behaviour can be understood as follows. At time zero, the lithosphere–sticky air interface (dashed line in Fig. 10) is prescribed as a flat line. However, the finite and irregular distances

Table 3. Temporal resolution test.

Time step (a)	Max. topography ^a (m)	Topo. difference ^b (m)
4000	378	-20
2000	380	-18
1000	381	-17
500	395	-3
250	397	-1

Note: Uniform resolution: 601×201 nodes, 4×4 marker/cell.

Sticky air: $h_{st} = 100$ km; $\eta_{st} = 10^{18}$ Pa s ($C_{Stokes} = 6.5 \times 10^{-4}$).

^aFor Case 2 at $t = 3$ Ma using the code I2VIS.

^bCompared to true free-surface result of MILAMIN_VEP (398 m).

between markers constrain the interface only within a finite irregular band. Adopting a tentative ‘uncertainty principle’ the position of the interface is uncertain, and its most probable position may be found by formulating a condition of optimizing equal distances to nearby markers of different type (lithosphere or sticky air). This position of the virtual sticky air interface is indicated by the red curve in Fig. 10(a). This irregular interface is associated with irregular buoyancy forces at the gridpoints, leading to small velocity

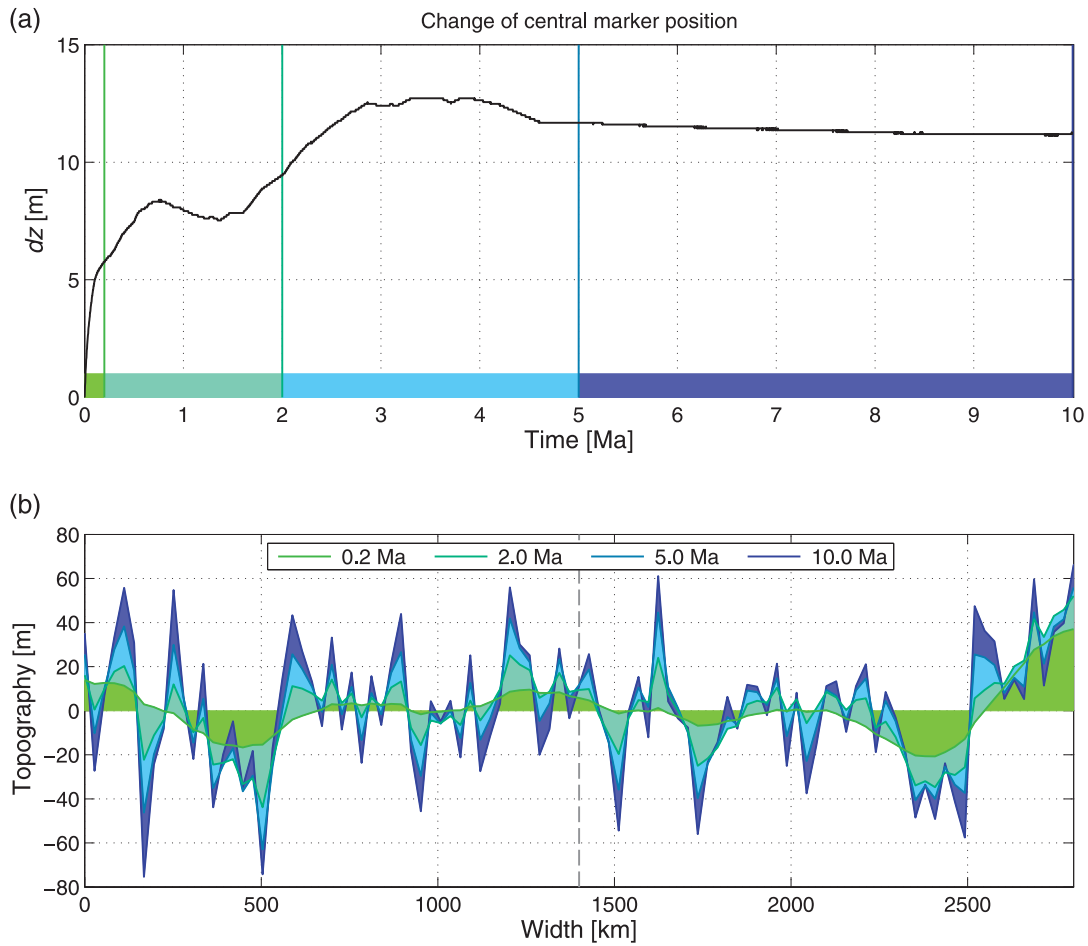


Figure 9. Evolution of the surface of the lithosphere of Case 2, but without a buoyant cylinder, that is, without any driving force. (a) Vertical position of one marker (at central position indicated by the vertical, dashed line Fig. 9b) at the surface of the lithosphere with time, (b) topography profiles after 200 ka, 2 Ma, 5 and 10 Ma as also indicated by the vertical, coloured lines in Fig. 9a. (Calculated by FDCON using a sticky air configuration of $h_{st} = 100$ km and $\eta_{st} = 10^{19}$ Pa s.)

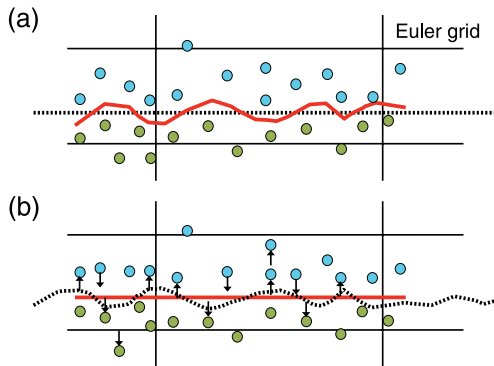


Figure 10. Sketch of tracer distribution at the boundary between lithosphere (green) and sticky air (cyan) showing the real interface (dashed line) and the virtual interface (red line) for (a) the initial and (b) the final setup after relaxation.

variations. These velocities displace the markers until complete relaxation is achieved and the virtual sticky air interface is flat (Fig. 10b). As a matter of fact, the initially prescribed flat interface (dashed curve) is displaced in opposite direction. Thus this effect resembles isostatic relaxation of an irregular interface, which has a relaxation time given by eq. (10), in which λ now is the wavelength

of the relaxing perturbation. Long wavelengths relax fastest, which is clearly depicted in Fig. 9b. Also the amplitude of the fluctuation of a given wavelength λ can be estimated, which is given by the mean half vertical distance between markers, $\Delta z_m/2$, reduced by a factor $1/\sqrt{\lambda/\Delta x_m}$, which results from horizontal averaging over approximately $\lambda/\Delta x_m$ markers. Thus, we get the final amplitude of the fluctuations of a certain wavelength of the following order of magnitude:

$$h_{\text{fluct}} = O\left(\frac{\Delta z_m \sqrt{\Delta x_m}}{2\sqrt{\lambda}}\right). \quad (27)$$

This estimate gives 60 m for the parameters of the model shown in Fig. 9, which is in good agreement with the numerical amplitudes. Eq. (27) gives us a good rule of how to minimize the fluctuations: the vertical distance needs to be chosen smaller than the horizontal distance.

Another way of preventing these fluctuations is to discretize the free surface (dashed line in Fig. 10) with the help of a marker chain. The viscosity of the nodal points above this chain can consequently be set to sticky air values. This method would further allow to easily implement more sophisticated erosion models to the code.

The accuracy of the sticky air models is locally (i.e. on the marker scale) in the order of the marker ‘uncertainty principle’. Depending on the number of markers in z -direction (nm_z), this results in errors

in the order of one one-thousandth for the whole model domain ($1/nm_z$). On the numerical grid scale this error is reduced by a factor $\sqrt{n_x/nm_x}$, as one has to average over (n_x/nm_x) marker positions. Thus, the numerical accuracy of the topography of the sticky air models is very high. Only if taken relative to the total topography the errors appear bigger and are in the order of 5–10 per cent for sticky air parameters around $C_{\text{isost}} > 0.1$ and in the order of 1–2 per cent for $C_{\text{isost}} < 0.1$.

5.5 True free surface versus sticky air approach

Two codes participating in our comparison, SULEC and UNDERWORLD, have a true free surface, but have also run the cases with a sticky air layer. Their experiences and results can, therefore, be used to discuss the advantages and disadvantages of the two methods. A true free surface obtained by adjusting the location of nodes within a structured grid with fixed connectivity combined with tracer tracking (such as in SULEC and UNDERWORLD), requires in principle few special considerations. Compared to fixed grid methods, the free-surface approaches are more computationally expensive. SULEC and UNDERWORLD employ a structured mesh with a fixed number of elements in each direction. The constant connectivity of the mesh implies that the same matrix non-zero structure can be reused at every time step. To redefine the node locations, SULEC vertically shifts the nodal coordinates at the free surface so that they conform to the free surface. The nodes below each surface node are adjusted, keeping the relative grid spacing in the vertical direction the same. UNDERWORLD employs a fully Lagrangian update of the free-surface coordinates. To ensure good mesh quality, a simple mesh smoothing algorithm is used to adjust the nodal coordinates within the domain. Because of the grid modification, these methods are computationally expensive and this is where fixed grid methods have a computational advantage.

The requirement of a vertically fixed surface boundary condition, however, necessitates an approximation to simulate a free surface, such as the sticky air method. Comparing a true free surface versus a sticky air in an ALE-type code, we find that the sticky air layer requires:

- (1) The ability to handle large viscosity contrasts at the surface (up to five orders of magnitude in our examples). However, this constraint becomes less severe when brittle deformation near the surface would be considered. Brittle strength is low at the surface, resulting in a smaller viscosity difference with the sticky air.
- (2) Tracking of the air–rock interface. SULEC uses a marker chain and the precision with which the air–rock interface is found depends on the marker chain advection and resolution. However, the precision of the true free-surface approach is determined by the spacing of the nodes of the Eulerian grid. We find that three marker chain particles per element are sufficient to resolve the air–rock interface to within the true free-surface position. UNDERWORLD does not explicitly track the free surface in the sticky air experiments. All material properties are defined using a set of markers, which provide a volumetric representation of the fluid.
- (3) Avoiding that the high velocities in the weak sticky air layer contribute to advection of the rock–air interface. To avoid deformation of the marker chain used in SULEC, the marker chain is placed slightly below the air–rock interface.
- (4) A high resolution in the sticky air layer. This is especially important near the air–rock interface and can be relaxed at larger

altitudes in the air layer. SULEC uses a vertical element size down to 250 m at the air–rock interface. This requirement can result in the sticky air solution becoming computationally expensive (e.g. in global convection models).

(5) Monitoring of markers that overshoot the air–rock interface (air-in-crust or crust-in-air) although this occurrence is not observed for all the codes. These need to be either reassigned or removed (potentially violating mass conservation).

It is important to keep in mind that a stabilization algorithm needs to be applied to both a true free surface and the air–rock interface (Kaus *et al.* 2010; Quinquis *et al.* 2011). It is the density difference that requires the stabilization, so using a sticky-air layer does not overcome the stabilization requirement. Duretz *et al.* (2011), however, demonstrated that it is possible to add a stabilization method to finite difference formulations in a straightforward manner as well without loss of solution accuracy.

Which approach to prefer, a true free surface or a sticky-air layer, depends on the problem at hand and the tools that are available. Studies that focus on small-scale structures near the surface (on the order of a few kilometres or less) are probably better off using a true free surface, due to the strict requirements on tracking and resolution. Studies that focus on structures at deep mantle depths can reach a more than sufficient approximation to a free surface with a relatively coarse (and therefore not so expensive) sticky air layer.

5.6 Application

The conversion from a free-slip surface to a physical more appropriate free surface can easily be implemented by the addition of a sticky air layer and without changing boundary conditions. This work presents the application of a free-surface approach using the sticky air for two simple cases of geodynamic processes occurring in a terrestrial planet. The list of possible geodynamic applications is long and ranges from global terrestrial modelling to regional scale geodynamics. For general cases, the dominant driving term of the system should be evaluated to derive a prediction on the magnitude of surface movements (i.e. the maximum vertical velocity). Thereby, this might be the sinking velocity of a slab or the Stokes velocity of a rising plume in dynamic models or it might be given by the prescribed velocity in kinematic models.

Using such an analytical prediction for maximum velocity, it is possible to derive an individual C -condition from eq. (7) that is adapted to the special model of interest. Suitable sticky air properties can, therefore, be easily computed. Moreover, they could be monitored during a simulation by solving and monitoring the general expression given in eq. (7) for the current maximum surface velocity to ensure a proper topography evolution.

Although the present cases have been isothermal, the question arises how to handle thermal effects in the case of thermomechanical modelling. Here, we briefly mention possible approaches without going into detail. (i) After solving the heat equation at each time step in the full region including sticky air, the temperature can be artificially set to a constant value (the surface temperature) everywhere in the sticky air region. (ii) The heat conductivity of the sticky air can be increased artificially by several orders of magnitude to mimic advective heat transport through the sticky air. In this case, care has to be taken to guarantee that the heat equation solver tolerates sharp conductivity contrasts, that is, an anisotropic marker distribution suppresses the fluctuations.

6 CONCLUSION

Topography and surface evolution approached from numerical models is a field in development and requires careful treatment. We, therefore, compared three approaches to compute numerical surface topography. We find that non-flexible surface boundary models, which compute a traction derived topography, successfully predict dynamic and isostatic topography if the topography is small compared to the model dimensions and if in addition topographic slopes are small. The method fails to predict (i) the time-dependent relaxation into isostatic equilibrium, (ii) short term ($< t_{\text{fix}}$) topography variations and (iii) the topography resulting from viscous plate bending. On the contrary, the sticky air method is a good way to simulate a free surface for Eulerian approaches, provided that its parameters are chosen carefully. Eqs (12) and (18) give framework conditions for a suitable sticky air application when $C \ll 1$, for short term isostatic relaxation and long-term geodynamics, respectively. Numerically feasible thick layers of low viscosity using for example, 50 km with 10^{18} Pa s up to 500 km with 10^{20} Pa s give good results not only for long term but also for short-term surface movements. A general C -condition is further provided by eq. (7) to check any given model setup using its maximum driving term (i.e. the max. surface velocity). In this work, the sticky air layer is vertically covered by at least four gridpoints (see supplementary Table S1), which yields acceptable results. Spurious lateral fluctuations of topography as observed in some marker-based sticky air approaches may effectively be damped by an anisotropic distribution of markers with a higher order of marker number per element in vertical than in horizontal direction (eq. 27) or by using marker chains to track the air–subsurface interface.

ACKNOWLEDGMENTS

FC and TD are supported by SNF grant 20TO21-120535 as part of the TOPO-EUROPE program. SB acknowledges support by the Norwegian Research Council (grant 180449). DAM was supported by the ETH Zürich Postdoctoral Fellowship Program and BJKP by ERC Starting Grant 258830. We thank S.D. King and S. Zhong for constructive comments.

REFERENCES

- Balay, S. *et al.*, 2008. *PETSc Users Manual*, Technical Report ANL-95/11 - Revision 3.0.0, Argonne National Laboratory, <http://www.mcs.anl.gov/petsc/petsc-current/docs/manual.pdf>.
- Beaumont, C., Fullsack, P. & Hamilton, J., 1994. Styles of crustal deformation in compressional orogens caused by subduction of the underlying lithosphere, *Tectonophysics*, **232**(1–4), 119–132.
- Blankenbach, B. *et al.*, 1989. A benchmark comparison for mantle convection codes, *Geophys. J. Int.*, **98**(1), 23–38.
- Braun, J., 2006. Recent advances and current problems in modelling surface processes and their interaction with crustal deformation, in *Analogue and Numerical Modelling of Crustal-Scale Processes*, Geol. Soc. Lond. Spec. Publ. Vol. 253, pp. 307–325, eds Uiter, S.J.H.B. & Schreurs, G., The Geological Society, London, doi:10.1144/GSL.SP.2006.253.01.16.
- Braun, J. & Yamato, P., 2010. Structural evolution of a three-dimensional, finite-width crustal wedge, *Tectonophysics*, **484**(1–4), 181–192.
- Braun, J., Thieulot, C., Fullsack, P., DeKool, M., Beaumont, C. & Huismans, R., 2008. DOUAR: a new three-dimensional creeping flow numerical model for the solution of geological problems, *Phys. Earth planet. Inter.*, **171**(1–4), 76–91.
- Burkett, E.R. & Billen, M.I., 2009. Dynamics and implications of slab detachment due to ridge-trench collision, *J. geophys. Res.*, **114**(B12), B12402, doi:10.1029/2009JB006402.
- Crook, A.J.L., Willson, S.M., Yu, J.G. & Owen, D.R.J., 2006. Predictive modelling of structure evolution in sandbox experiments, *J. Struct. Geol.*, **28**(5), 729–744.
- Dabrowski, M., Krotkiewski, M. & Schmid, D.W., 2008. MIL-AMIN: MATLAB-based finite element method solver for large problems, *Geochem. Geophys. Geosyst.*, **9**(4), Q04030, doi:10.1029/2007GC001719.
- Duret, T., May, D.A., Gerya, T.V. & Tackley, P.J., 2011. Discretization errors and free surface stabilization in the finite difference and marker-in-cell method for applied geodynamics: a numerical study, *Geochem. Geophys. Geosyst.*, **12**(7), Q07004, doi:10.1029/2011GC003567.
- Fuchs, L., Schmeling, H. & Koyi, H., 2011. Numerical models of salt diapir formation by down-building: the role of sedimentation rate, viscosity contrast, initial amplitude and wavelength, *Geophys. J. Int.*, **186**(2), 390–400.
- Fullsack, P., 1995. An arbitrary Lagrangian-Eulerian formulation for creeping flows and its application in tectonic models, *Geophys. J. Int.*, **120**(1), 1–23.
- Gerya, T.V. & Yuen, D.A., 2003a. Rayleigh-Taylor instabilities from hydration and melting propel ‘cold plumes’ at subduction zones, *Earth planet. Sci. Lett.*, **212**(1–2), 47–62.
- Gerya, T.V. & Yuen, D.A., 2003b. Characteristics-based marker-in-cell method with conservative finite-differences schemes for modeling geological flows with strongly variable transport properties, *Phys. Earth planet. Inter.*, **140**(4), 293–318.
- Gurnis, M., Eloy, C. & Zhong, S., 1996. Free-surface formulation of mantle convection—II. implication for subduction-zone observables, *Geophys. J. Int.*, **127**(3), 719–727.
- Hager, B.H., Clayton, R.W., Richards, M.A., Comer, R.P. & Dziewonski, A.M., 1985. Lower mantle heterogeneity, dynamic topography and the geoid, *Nature*, **313**(6003), 541–546.
- Harlow, F.H. & Welsh, J.E., 1965. Numerical calculation of time-dependent viscous incompressible flow of fluid with free surface, *Phys. Fluids*, **8**(10), 2182–2189.
- Hassani, R. & Chéry, J., 1996. Anelasticity explains topography associated with basin and range normal faulting, *Geology*, **24**(12), 1095–1098.
- Kaus, B.J.P. & Becker, T.W., 2007. Effects of elasticity on the Rayleigh–Taylor instability: implications for large-scale geodynamics, *Geophys. J. Int.*, **168**(2), 843–862.
- Kaus, B.J.P., Steedman, C. & Becker, T.W., 2008. From passive continental margin to mountain belt: insights from analytical and numerical models and application to Taiwan, *Phys. Earth planet. Inter.*, **171**(1–4), 235–251.
- Kaus, B.J.P., Mühlhaus, H. & May, D.A., 2010. A stabilization algorithm for geodynamic numerical simulations with a free surface, *Phys. Earth planet. Inter.*, **181**(1–2), 12–20.
- King, S.D., 2009. On topography and geoid from 2-d stagnant lid convection calculations, *Geochem. Geophys. Geosyst.*, **10**(3), Q03002, doi:10.1029/2008GC002250.
- Koons, P.O., 1989. The topographic evolution of collisional mountain belts: a numerical look at the Southern Alps, New Zealand, *Am J Sci*, **289**(9), 1041–1069.
- Lavier, L.L., Buck, W.R. & Poliakov, A.N.B., 2000. Factors controlling normal fault offset in an ideal brittle layer, *J. geophys. Res.*, **105**(B10), 23 431–23 442.
- McKenzie, D., 1977. Surface deformation, gravity anomalies and convection, *Geophys. J. R. astr. Soc.*, **48**(2), 211–238.
- Melosh, H.J. & Raefsky, A., 1980. The dynamical origin of subduction zone topography, *Geophys. J. R. astr. Soc.*, **60**(3), 333–354.
- Moresi, L., Dufour, F. & Mühlhaus, H.-B., 2003. A Lagrangian integration point finite element method for large deformation modeling of viscoelastic geomaterials, *J. Comput. Phys.*, **184**(2), 476–497.
- Moresi, L., Quenette, S., Lemiale, V., Mériaux, C., Appelbe, B. & Mühlhaus, H.-B., 2007. Computational approaches to studying non-linear dynamics of the crust and mantle, *Phys. Earth planet. Inter.*, **163**(1–4), 69–82.
- Mühlhaus, H., Bourguoin, L. & Hale, A., 2007. Free surface modeling based on level sets, *ICCES*, **3**(4), 225–232.

- Pelletier, D., Fortin, A. & Camarero, R., 1989. Are FEM solutions of incompressible flows really incompressible? (or how simple flows can cause headaches!), *Int. J. Numer. Methods Fluids*, **9**(1), 99–112.
- Poliakov, A. & Podladchikov, Y., 1992. Diapirism and topography, *Geophys. J. Int.*, **109**(3), 553–564.
- Pysklywec, R.N., Beaumont, C. & Fullsack, P., 2000. Modeling the behavior of the continental mantle lithosphere during plate convergence, *Geology*, **28**(7), 655–658.
- Quinquis, M.E.T., Buitter, S.J.H. & Ellis, S., 2011. The role of boundary conditions in numerical models of subduction zone dynamics, *Tectonophysics*, **497**(1–4), 57–70.
- Quinteros, J., Ramos, V.A. & Jacovkis, P.M., 2009. An elasto-visco-plastic model using the finite element method for crustal and lithospheric deformation, *J. Geodyn.*, **48**(2), 83–94.
- Ramberg, H., 1967. *Gravity, Deformation, and the Earth's Crust: In Theory, Experiments and Geological Application*, Academic Press, London, 214pp.
- Samuel, H. & Evonuk, M., 2010. Modeling advection in geophysical flows with particle level sets, *Geochem. Geophys. Geosyst.*, **11**(8), Q08020, doi:10.1029/2010GC003081.
- Schenk, O. & Gärtner, K., 2004. Solving unsymmetric sparse systems of linear equations with PARDISO, *Future Gener. Comput. Syst.*, **20**(3), 475–487.
- Schmeling, H. & Marquart, G., 1991. The influence of second-scale convection on the thickness of continental lithosphere and crust, *Tectonophysics*, **189**(1–4), 281–306.
- Schmeling, H. *et al.*, 2008. A benchmark comparison of spontaneous subduction models—towards a free surface, *Phys. Earth planet. Inter.*, **171**(1–4), 198–223.
- Tackley, P.J., 1993. Effects of strongly temperature-dependent viscosity on time-dependent, three-dimensional models of mantle convection, *Geophys. Res. Lett.*, **20**(20), 2187–2190.
- Tackley, P.J., 2008. Modelling compressible mantle convection with large viscosity contrasts in a three-dimensional spherical shell using the yin-yang grid, *Phys. Earth planet. Inter.*, **171**(1–4), 7–18.
- Tackley, P.J. & King, S.D., 2003. Testing the tracer ratio method for modeling active compositional fields in mantle convection simulations, *Geochem. Geophys. Geosyst.*, **4**(4), 8302, doi:10.1029/2001GC000214.
- Turcotte, D. & Schubert, G., 2002. *Geodynamics*, 2nd edn, Cambridge University Press, New York, NY.
- Weinberg, R.F. & Schmeling, H., 1992. Polydiapirs: multiwavelength gravity structures, *J. Struct. Geol.*, **14**(4), 425–436.
- Willett, S.D., 1999. Orogeny and orography: the effects of erosion on the structure of mountain belts, *J. geophys. Res.*, **104**(B12), 28 957–28 981.
- Zaleski, S. & Julien, P., 1992. Numerical simulation of Rayleigh-Taylor instability for single and multiple salt diapirs, *Tectonophysics*, **206**(1–2), 55–69.
- Zhong, S., 2002. Effects of lithosphere on the long-wavelength gravity anomalies and their implications for the formation of the Tharsis rise on Mars, *J. geophys. Res.*, **107**(E7), 5054, doi:10.1029/2001JE001589.
- Zhong, S. & Gurnis, M., 1992. Viscous flow model of a subduction zone with a faulted lithosphere: long and short wavelength topography, gravity and geoid, *Geophys. Res. Lett.*, **19**(18), 1891–1894.
- Zhong, S., Gurnis, M. & Hulbert, G., 1993. Accurate determination of surface normal stress in viscous flow from a consistent boundary flux method, *Phys. Earth planet. Inter.*, **78**(1–2), 1–8.
- Zhong, S., Gurnis, M. & Moresi, L., 1996. Free-surface formulation of mantle convection—I. Basic theory and application to plumes, *Geophys. J. Int.*, **127**(3), 708–718.

SUPPORTING INFORMATION

Additional Supporting Information may be found in the online version of this article:

Table S1. Results.

Please note: Wiley-Blackwell are not responsible for the content or functionality of any supporting materials supplied by the authors. Any queries (other than missing material) should be directed to the corresponding author for the article.